Global Microwave Satellite Observations of Sea Surface Temperature for Numerical Weather Prediction and Climate Research

BY DUDLEY B. CHELTON AND FRANK J. WENTZ

New satellite microwave observations provide global sea surface temperature fields every 2 days with approximately 50-km resolution in near-all-weather conditions.

S ea surface temperature (SST) influences the atmosphere through its effects on sensible and latent heat fluxes across the air–sea interface and is therefore fundamentally important for climate research and for accurate simulations of surface and low-level winds in numerical weather prediction (NWP) models. On large scales, SST is negatively correlated with surface winds, which has been interpreted as evidence of one-way forcing of the ocean by the atmosphere through wind effects on air–sea heat fluxes and Ekman advection of the mean SST gradients (e.g., Mantua et al. 1997; Okumura et al. 2001; Tomita et al. 2002; Visbeck et al. 2003). On scales of 100–3000 km in regions of strong SST fronts associ-

ated with ocean currents, recent satellite observations of SST and surface winds reveal fundamentally different ocean–atmosphere interaction (Xie 2004; Chelton et al. 2004). In these regions, SST and surface winds are positively correlated from SST-induced changes in the stability of the atmospheric boundary layer that modify the low-level winds through their effects on vertical turbulent mixing. The persistence of the ocean–atmosphere heat fluxes that sustain this small-scale SST forcing of low-level winds is evidently attributable to oceanic advective and eddy heat fluxes that maintain the warm and cool SST anomalies associated with meandering ocean currents. The importance of this oceanic forcing of the atmosphere to climate variability is not yet known because scales smaller than ~1000 km are poorly resolved in climate datasets. The global satellite microwave observations of SST that have been available since June 2002 from the Advanced Microwave Scanning Radiometer on the National Aeronautics and Space Administration (NASA) Earth Observing System (EOS) *Aqua* satellite (AMSR-E) are introduced here and evaluated for climate research and NWP applications.

The observed SST influence on the surface wind field is clearly identifiable in NWP models, albeit with underestimated intensity (Chelton 2005). The

AFFILIATIONS: CHELTON—College of Oceanic and Atmospheric Sciences, Oregon State University, Corvallis, Oregon; WENTZ—Remote Sensing Systems, Santa Rosa, California
CORRESPONDING AUTHOR: Dudley B. Chelton, College of Oceanic and Atmospheric Sciences, 104 COAS Administration Building, Oregon State University, Corvallis, OR 97331-5503
E-mail: chelton@coas.oregonstate.edu

second objective of this study is to demonstrate the sensitivity of NWP models and, by inference, climate models, to specification of the SST boundary condition. This is accomplished by analyzing surface wind stress fields from the European Centre for Medium-Range Weather Forecasts (ECMWF) operational NWP model and is made possible by the fact that a major change in the SST boundary condition was implemented in May 2001. Prior to this time, the SST boundary condition consisted of the 7-day-averaged Reynolds SST analyses (Reynolds and Smith 1994; Reynolds et al. 2002). At 1800 UTC 9 May 2001, ECMWF changed the ocean boundary condition to the 1-day-averaged, higher spatial resolution Real-Time Global SST (RTG_SST) analyses that have been produced operationally since 30 January 2001 by the National Oceanic and Atmospheric Administration (NOAA; Thiébaux et al. 2003).

The paper begins with an overview of satellite measurements of SST, including brief summaries of the Reynolds and RTG_SST analyses that are based on a blending of in situ observations and satellite infrared measurements from the Advanced Very High Resolution Radiometer (AVHRR). Regional examples of 3-day composite averages of AVHRR, RTG_SST, and AMSR-E data, and the nearest corresponding weekly average Reynolds SST analyses are then presented for six areas of the World Ocean to summarize the resolution limitations of the Reynolds and RTG_SST analyses. The importance of accurate specification of the SST boundary condition in NWP and climate models is investigated from analyses of surface wind stress fields constructed from the ECMWF and the NOAA National Centers for Environmental Prediction (NCEP) models. The paper concludes with a summary of the results and a discussion of how AMSR-E data could be used to improve the accuracy of SST and wind stress fields for NWP and climate research.

SATELLITE-BASED GLOBAL SST FIELDS.
Because of the sparse coverage of in situ measurements of SST from buoys and ships, satellite observations are essential for construction of global SST fields. Historically, satellite measurements of SST have been provided by the AVHRR with multiple infrared channels that has been operational on NOAA satellites since November 1981. Infrared (IR)

measurements of SST can only be obtained in cloud-free conditions. Cloud contamination[1] is particularly problematic over the subpolar oceans where cloud cover can exceed 75%. Infrared estimates of SST are also contaminated by aerosols from volcanic eruptions and dust storms (Diaz et al. 2001).

Because clouds and aerosols are essentially transparent to microwave radiation at frequencies below about 12 GHz, microwave remote sensing has the potential to eliminate the atmospheric contamination problems that plague IR measurements. The atmospheric contribution to the microwave brightness temperatures measured by a satellite at these frequencies is only a few percent. Microwave estimates of SST are possible because the surface radiance is proportional to SST at frequencies between about 4 and 12 GHz. SST retrievals at these frequencies must also take into account the effects of wind on the emissivity of the sea surface. Since microwave emission from the sea surface is weak, accurate satellite microwave observations of SST require a highly calibrated radiometer. High-quality microwave SST data first became available in December 1997 from measurements at 10.7 GHz by the Tropical Rainfall Measuring Mission (TRMM) Microwave Imager (TMI; Wentz et al. 2000). Individual TMI observations of SST have a footprint size of about 46 km and an accuracy of about 0.5°C (see the appendix).

While the 46-km footprint size of TMI measurements of SST is large compared with the ~1 km footprint of satellite IR observations, the microwave data have the considerable advantage that the measurements are available in all nonraining conditions. Rain-contaminated measurements from TMI are identified and eliminated from further analysis using collocated measurements at 37 GHz. A limitation in coastal regions is that the TMI brightness temperatures are contaminated by land in the antenna side lobes within about 50 km of land.

As reviewed by Xie (2004), the TMI data have been used extensively in studies of air–sea interaction in the tropical latitudes of all three ocean basins. TMI measurements of SST, together with simultaneous measurements of surface winds by the Quick Scatterometer (QuikSCAT), revealed that the coupling between the ocean and the atmospheric boundary layer on scales smaller than a few thousand kilometers in regions of

---

[1] Cloud contamination of IR measurements can be difficult to identify unambiguously. As a consequence, automated cloud-screening algorithms sometimes fail to identify clouds and sometimes falsely identify clear areas as cloud covered (e.g., Cayula and Cornillon 1996; Stowe et al. 1999; Di Vittorio and Emery 2002).

strong SST fronts is much stronger than had been inferred previously from sparse in situ observations.

Aside from the larger footprint size compared with IR and the inability to measure SST near land, the primary limitation of TMI data is the low inclination of the TRMM orbit, which restricts the TMI observations to the latitude band of 40°S–40°N. This precludes studies of SST influence on surface winds over oceanographically important midlatitude SST fronts. In addition, the SST sensitivity of the TMI 10.7-GHz brightness temperatures decreases with decreasing SST, resulting in degraded accuracy of TMI retrievals of SST below about 10°C.

Both the restricted latitudinal sampling and the degraded accuracy of TMI estimates at low SST are eliminated in the SST measurements by the AMSR-E, which orbits the Earth on the EOS *Aqua* satellite in a sun-synchronous, near-polar orbit. The AMSR-E has sampled the global ocean since 1 June 2002 with 89% coverage each day and 98% coverage every 2 days. AMSR-E retrievals of SST (see the appendix) are based on measurements of brightness temperature at 6.9 GHz, which is more sensitive to SST than are the 10.7-GHz measurements used in TMI retrievals, particularly at the low temperatures at which TMI retrievals become degraded. Rain-contaminated measurements are identified and excluded from further analysis using collocated measurements at 36.5 GHz. The AMSR-E footprint size for SST measurements is about 56 km, and the accuracy is estimated to be about 0.4°C (see the appendix). Sidelobe contamination at 6.9 GHz with the AMSR-E antenna extends about 75 km

from land and ice, both of which are easily identified as brightness temperatures that are considerably warmer and less polarized than ocean brightness temperatures.

The improved global sampling of microwave measurements of SST by AMSR-E compared with IR measurements by the AVHRR is evident in Fig. 1, which shows the percent coverage for each instrument in 3-day composite averages of SST over the 12-month period October 2002 through September 2003, during which there was no significant loss of AMSR-E data. The low coverage at high latitudes is attributable to ice cover. At lower latitudes, the prevalence of rain contamination reduced the AMSR-E coverage to 85% in the intertropical convergence zone near 10°N in the
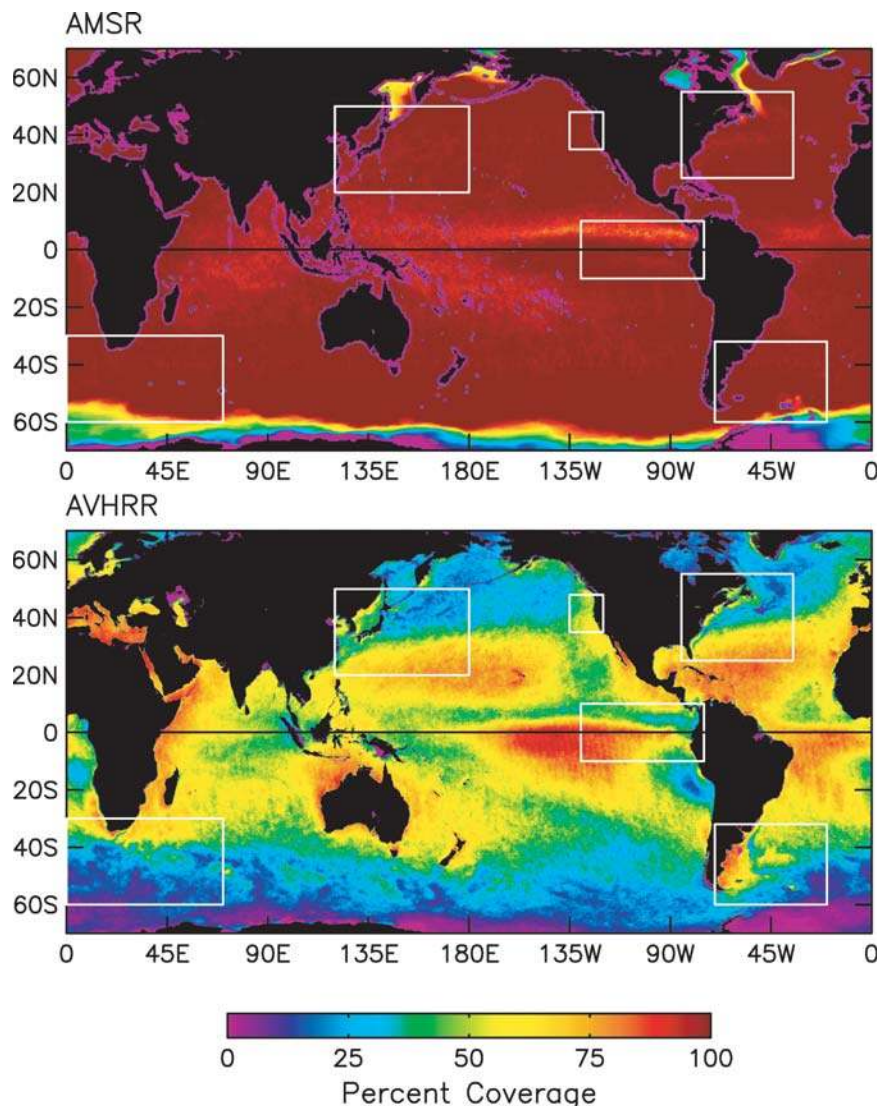

FIG. 1. Percent coverage of SST measurements from (top) the AMSR-E and (bottom) the AVHRR in 3-day composite average maps during the 12-month period Oct 2002 through Sep 2003. The white boxes indicate the six areas for which example 3-day-averaged SST maps are presented in Figs. 4 and 6–10.

eastern and central Pacific and to about 90% in some regions of the tropical Atlantic and Indian Oceans. Elsewhere, AMSR-E coverage in 3-day averages was near 100% everywhere. In comparison, AVHRR coverage in 3-day averages exceeds 75% in some regions of the Tropics and subtropics but is less than 30% over much of the middle- and high-latitude ocean.

TMI and AMSR-E measurements of SST are not presently utilized in the SST fields constructed for NWP or climate research since the data have only recently become available. Because the AVHRR measurements of SST have been available since November 1981, considerable effort has been devoted to their use for constructing global SST fields. Biases in AVHRR estimates of SST from incomplete corrections for cloud and aerosol contamination are reduced by blending the AVHRR measurements of SST with all available in situ data. The problems of sparse sampling of both the in situ and the AVHRR data over much of the World Ocean are dealt with by smoothing in both time and space.

Climate studies have traditionally been based on the Reynolds SST analyses (Reynolds and Smith 1994; Reynolds et al. 2002) produced operationally since 1981 by NOAA. The Reynolds SST analyses consist of weekly averages on a global 1° latitude × 1° longitude grid and are obtained from a nonlinear iterative objective analysis (OA) that uses correlation length scales of approximately 900 km zonally and 600 km meridionally.

Until recently, the Reynolds SST analyses have also been the only global SST fields available for providing the ocean boundary condition in operational NWP models. On 30 January 2001, NOAA began producing new operational high-resolution SST fields, referred to as the RTG_SST analyses (Thiébaux et al. 2003). The RTG_SST analyses are provided as daily averages on a 0.5° latitude × 0.5° longitude grid from a variational analysis that blends in situ and AVHRR measurements of SST. Large-scale biases in the satellite data are removed by the same method used in the Reynolds analyses. The RTG_SST analysis system was modified on 23 April 2002 to include a small amount of spatial smoothing of the daily average SST fields to reduce small-scale noise in the analyses (B. Katz 2003, personal communication).

The in situ and AVHRR data used to construct the RTG_SST analyses are the same as those used in the Reynolds analyses. In addition to the different gridding and temporal averaging summarized above, the two OA procedures differ significantly in the specification of the correlation length scales. The Reynolds analyses are based on the previously noted anisotropic correlation length scales of about 900 km zonally and 600 km meridionally. The RTG_SST analyses are based on geographically varying isotropic correlation length scales that are inversely proportional to the magnitude of the climatological average SST gradient magnitude, ranging from 100 km for regions of strong SST gradients to 450 km for regions of weak SST gradients (Thiébaux et al. 2003).

The improved spatial resolution of the RTG_SST analyses over the Reynolds analyses can be inferred from Fig. 2, which shows the root-mean-square (rms) differences between 7-day-averaged RTG_SST and Reynolds SST fields over the 12-month period October 2002 through September 2003. The rms differences are less than 0.25°C in the subtropical regions of weak SST gradients. In regions of strong SST gradients, such as the Kuroshio Extension in the North Pacific, the Gulf Stream in the northwest Atlantic, and in several regions of the Southern Ocean, the rms
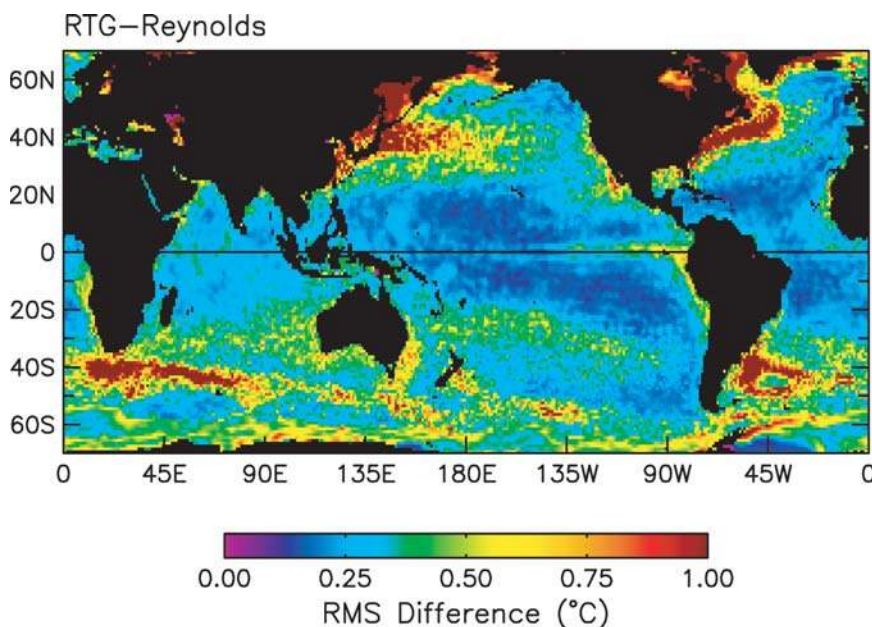

Fig. 2. Geographical distribution of the rms differences between 7-day averages of Reynolds and RTG_SST analyses of SST on a 1° lat × 1° lon grid over the 12-month period Oct 2002 through Sep 2003.

differences exceed 1°C. The higher spatial resolution of the RTG_SST fields is further illustrated from the example SST maps in the next section.

REGIONAL EXAMPLES OF SST. The potential of AMSR-E data to benefit climate research and NWP is illustrated in this section from example maps of SST from AVHRR data[2] (see online at ftp://podaac.jpl.nasa.gov/pub/sea_surface_temperature/avhrr/pathfinder/data_v5/), Reynolds analyses, RTG_SST analyses, and AMSR-E data[3] (see online at www.remss.com/amsr/) for the six areas shown by the white rectangles in Fig. 1. The times for which the SST maps are plotted for each area are indicated by the vertical dashed lines in the time series of percent coverage by AMSR-E and AVHRR in Fig. 3. These times were chosen somewhat arbitrarily to coincide with interesting features in the AMSR-E SST fields. The AVHRR, RTG_SST, and AMSR-E SST fields in these examples were constructed from 3-day composite averages. The Reynolds SST fields are the 7-day-averaged

analyses nearest in time to the center date of the 3-day averages of AVHRR, RTG_SST, and AMSR-E.

A 1-yr animation (October 2002–September 2003) of daily overlapping 3-day-average maps of AMSR measurements of SST for the region 62°S–70°N, 150°W–65°E centered on the Atlantic Ocean can be viewed at DOI:10.1175/BAMS-86-8-Chelton. This geographical region encompasses five of the six individual areas considered in this study plus several other interesting areas not specifically considered here.

The eastern tropical Pacific. Microwave SST observations from the TMI have been analyzed extensively over the past 5 yr in the eastern tropical Pacific where

---

[2] The AVHRR data used in this study consist of version 5.0 of the Pathfinder data produced by the Jet Propulsion Laboratory. These SST data include both daytime and nighttime measurements from the AVHRRs on all available NOAA satellites, averaged onto a 4-km global grid. For the present study, these SST fields were further averaged onto an 8-km global grid.

[3] The AMSR-E data used in this study are the version 4 data produced by Remote Sensing Systems on a 0.25° latitude × 0.25° longitude global grid, which is finer than the inherent 56-km resolution of individual SST measurements.
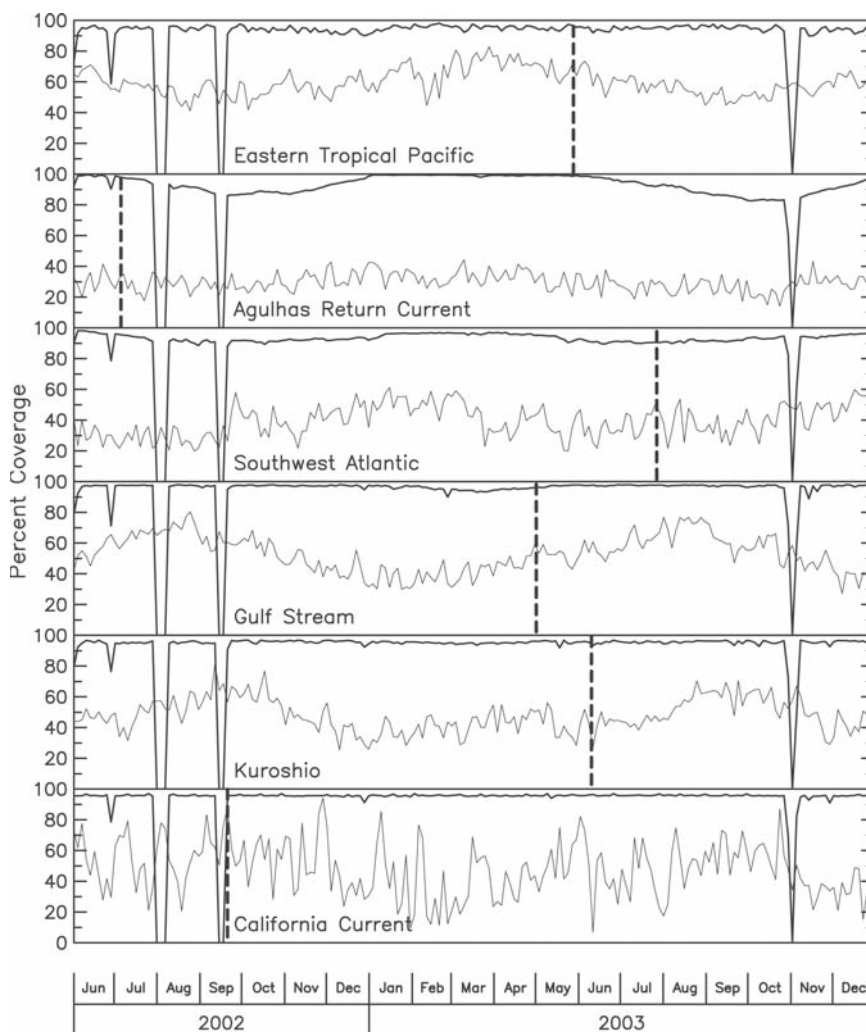

FIG. 3. Time series of the percent coverage from the AMSR-E (heavy lines) and the AVHRR (thin lines) for each of the regions shown in Figs. 4 and 6–10. The vertical dashed line in each panel indicates the time for which the corresponding map is shown in Figs. 4 and 6–10. The three periods of complete loss of AMSR-E data are due to EOS *Aqua* spacecraft anomalies during which the AMSR-E was not operational.

the variability on monthly time scales is dominated by tropical instability waves (TIWs). While TIWs have long been known to exist north of the equator in this region (Legeckis 1977; see also the review by Qiao and Weisberg 1995), the near-all-weather coverage of the TMI data revealed the existence of TIW-induced perturbations of the SST field south of the equator as well (Chelton et al. 2000). Together with measurements of surface wind stress by QuikSCAT, the TMI data also revealed the remarkably strong influence of SST on the atmospheric boundary layer in this region (Chelton et al. 2001; Hashizume et al. 2001). Perturbations of the wind stress, wind stress curl, and wind stress divergence fields all propagate synchronously westward at about 0.5 m s^{-1} with TIW-induced perturbations of the SST field. This

ocean–atmosphere coupling has also been observed from TMI and QuikSCAT data in the tropical Atlantic (Hashizume et al. 2001).

Example maps of SST in the eastern tropical Pacific for 28 May 2003 are shown in Fig. 4. The TMI map for this time (not shown here) is virtually indistinguishable from the AMSR-E map. The well-known equatorial cold tongue is readily apparent in all four of the left panels in Fig. 4. This cold tongue is present seasonally from about May through February in normal and La Niña years and weakens or disappears altogether during El Niño years. The undulating structure of the cold tongue is attributable to perturbations of the SST field by TIWs.

AVHRR observations of SST in the eastern tropical Pacific are limited by the fact that the skies are typically clear less than 50% of the time over the region just north of the northern flank of the cold tongue (Fig. 1). For the 3-day-averaging period shown in Fig. 4, during which the AVHRR coverage was better than average (Fig. 3), the skies were cloud covered on both sides of the cold tongue in the eastern portion of the AVHRR map with scattered clouds over the rest of the domain. The AVHRR nonetheless captured the undulating structure of the TIW perturbations of the cold tongue at this time. This structure is also apparent in the Reynolds SST field but is heavily smoothed. The undulating structure is better resolved in the RTG_SST map but is still significantly smoother than in either the AVHRR or the AMSR-E SST fields.

The resolution differences between the various SST fields are best seen from the maps of the magnitude of the SST gradient field in the right panels in Fig. 4. The SST gradients are about twice as strong in the RTG_SST map as in
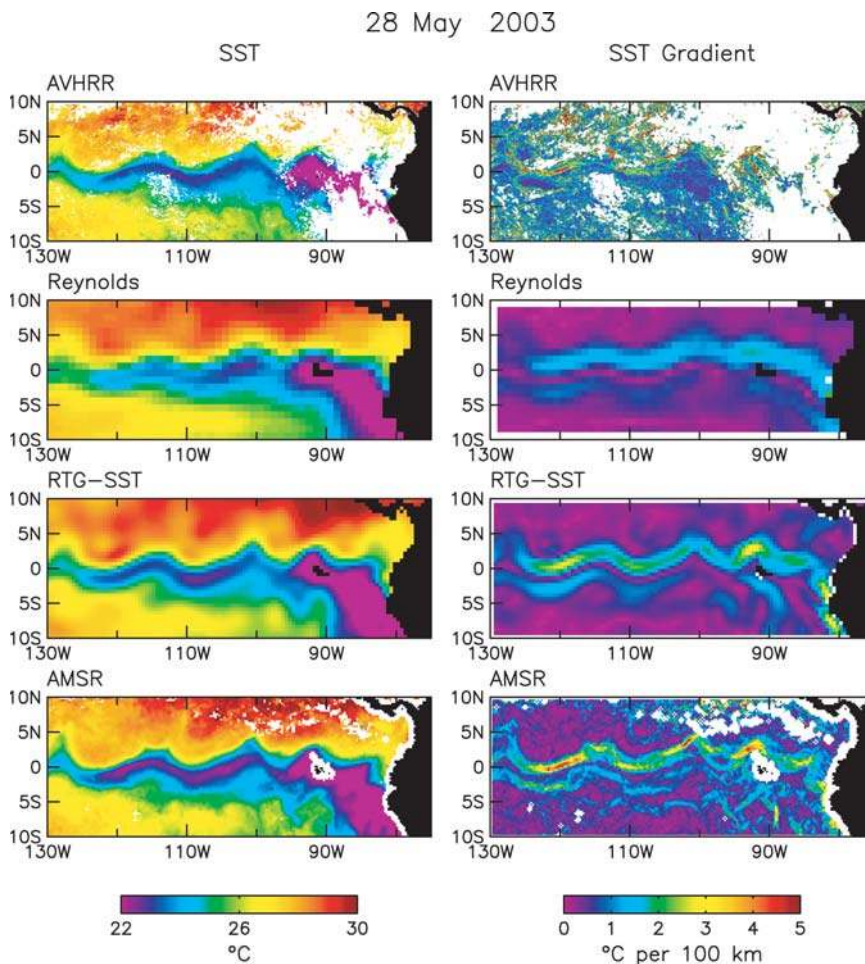

FIG. 4. Maps of (left) SST and (right) the magnitude of the SST gradient in the eastern tropical Pacific cold tongue region constructed from (top to bottom) AVHRR, Reynolds, RTG_SST, and AMSR-E for the 3-day-averaging period 27–29 May 2003. The white areas in the top left are regions of persistent cloud cover over the 3-day-averaging period. The white areas in the bottom left correspond to regions of rain contamination. These white areas expand in the derivative fields in the top right and bottom right panels.

the Reynolds map (upper-left panel in Fig. 5). The higher resolution of the RTG_SST fields significantly improved the accuracy of wind stress fields in the ECMWF model in this region after the May 2001 change from the Reynolds analyses to the RTG_SST analyses as the ocean boundary condition (Chelton 2005). While better than the Reynolds analyses, the SST gradients in the RTG_SST map are only 50% as strong as in the AMSR-E map (Fig. 5).

From comparison of the AMSR-E map with the clear-sky regions of the AVHRR map in Fig. 4, it can be noted that the SST gradients in this region are somewhat underestimated in intensity and overly smooth in the AMSR-E data. This is attributable to
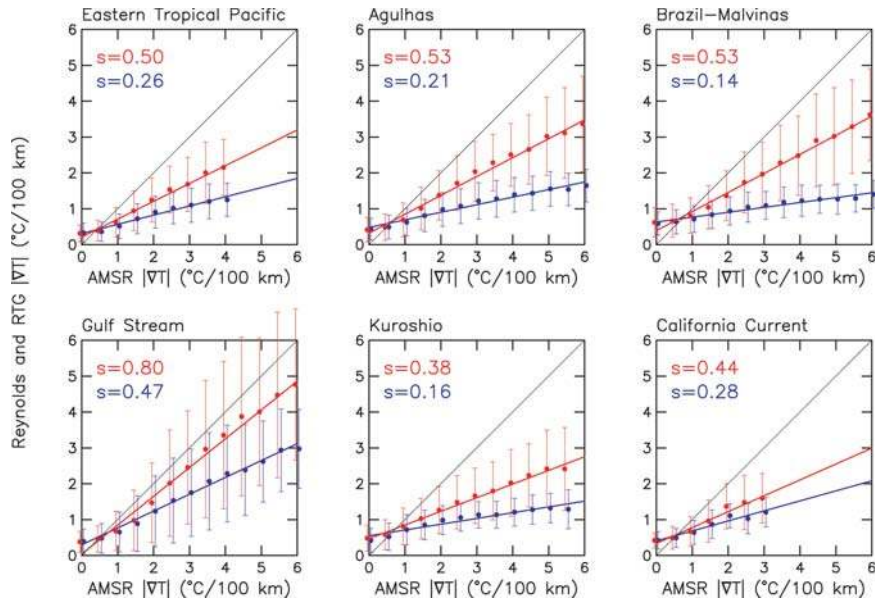

FIG. 5. Binned scatterplots of the magnitude of the SST gradients in the Reynolds (blue) and RTG_SST (red) fields as functions of the magnitude of the SST gradient in the AMSR-E SST field for the six regions shown in the maps in Figs. 4 and 6–10. The solid red and blue circles and associated vertical bars represent the average and ± std dev of the scatter of points within each bin. For display purposes, these binned values are offset slightly horizontally to avoid overlap of the std dev bars. The red and blue lines are least squares fits to the bin averages. The slopes s of these lines are labeled in the upper-left corner of each panel.

the resolution limitation of the 56-km footprint of the AMSR-E measurements. Also evident is the lack of AMSR-E data due to land contamination along the South and Central American coastlines and around the Galapagos and Marquesas Islands. Sporadic loss of AMSR-E data due to rain contamination is apparent near 5°N to the east of about 110°W. Overall, however, the 90%–95% AMSR-E coverage in this region is much better than the 40%–80% AVHRR coverage (Figs. 1 and 3). The lower spatial resolution of the AMSR-E data is thus a tradeoff for the much-improved spatial and temporal coverage compared with AVHRR data.

The Agulhas Return Current. In the southwest Indian Ocean, the Agulhas Current flows southward along the east coast of Africa to about 35°S, 25°E, where it separates from the coast, continues southwest to about 40°S, 20°E, and then abruptly retroflects eastward to form the Agulhas Return Current (ARC; Boebel et al. 2003). The 40°–45°S latitude of the meandering zonal SST front associated with the ARC is poleward of the highest latitude sampled by the TMI.

The first year of the AMSR-E data has been analyzed with simultaneous measurements of

wind stress by QuikSCAT to investigate ocean–atmosphere interaction in the ARC region (O'Neill et al. 2005). Compared with an earlier study based on Reynolds SST analyses (O'Neill et al. 2003), the AMSR-E data provided significantly improved characterization of the midlatitude influence of SST on the wind stress field. The coupling between SST and wind stress was found to be similar to that inferred in the eastern tropical Pacific from TMI and QuikSCAT data.

The limitations of the AVHRR observations are readily apparent from the maps for 5 July 2002 (Fig. 6). Undulations of the SST front are marginally visible along the northern flank of the ARC in the AVHRR map, but most of the sea surface at higher southern latitudes was obscured by clouds during this time period. This is typical of the AVHRR coverage in this region, which is less than 40% south of about 40°S (Fig. 1). Except for a rain cell near 45°S, 50°E, the AMSR-E coverage was virtually complete for this time period.

Not surprisingly, given the sparse coverage in both AVHRR and in situ observations of SST in this heavily cloud covered and remote region of the World Ocean, the Reynolds SST field in Fig. 6 is exceedingly smooth with no detectable undulations of the SST
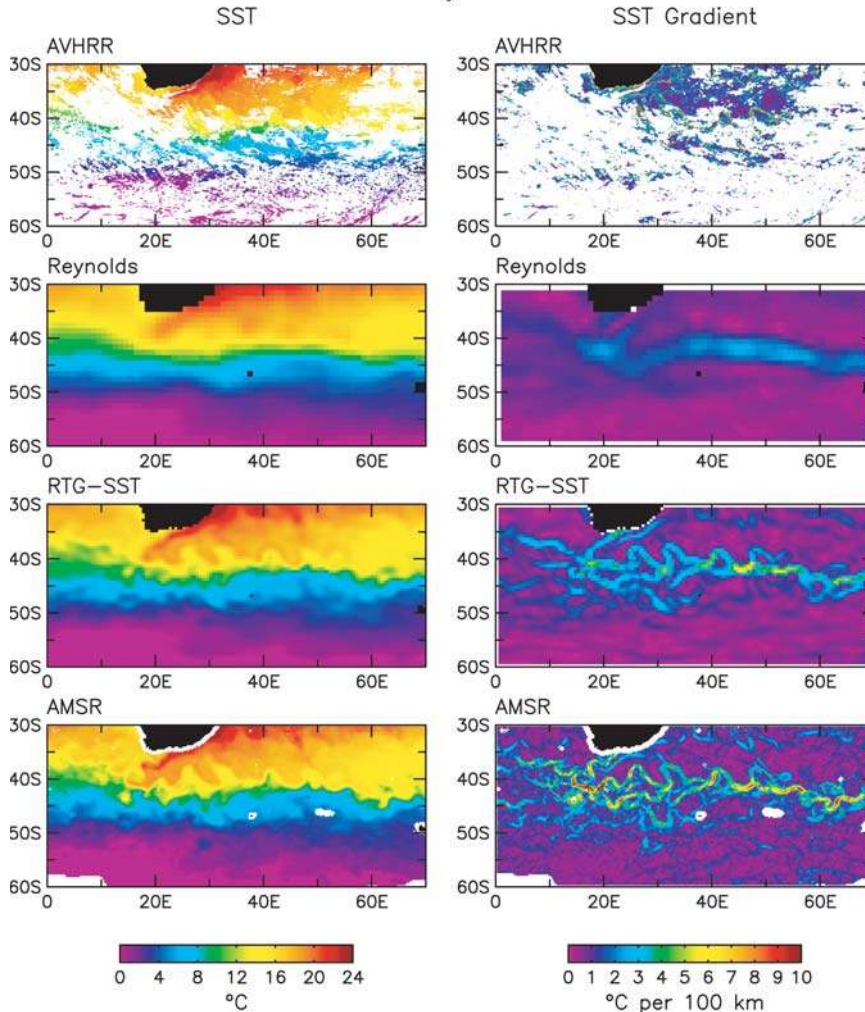
FIG. 6. Same as in Fig. 4, except for the ARC region of the southwest Indian Ocean for the 3-day-averaging period 4–6 Jul 2002.

with the confluence of the warm, southward-flowing Brazil Current and the cold, northward-flowing Malvinas Current (Saraceno et al. 2004). The interaction of these two currents results in strong temperature contrasts near the western boundary and large meanders and detached eddies throughout much of the interior basin. These features are all evident in the AMSR-E map of SST for 27 July 2003 (Fig. 7). Although the AVHRR coverage was better than average during this time period (Fig. 3), the southwest Atlantic was mostly cloud covered, limiting the utility of the AVHRR data.

As in the southwest Indian Ocean example in Fig. 6, the Reynolds SST analysis for the southwest Atlantic is exceedingly smooth. Despite the sparse coverage of in situ and AVHRR data in this region, the RTG_SST map captures the salient features, but it misses much of the detailed complex structure of the myriad SST fronts in this region. The resolution limitations are most clearly evident in the SST gradient maps in the right panels in Fig. 7. The SST gradients in the RTG_SST and Reynolds maps are only 53% and 14% as strong, respectively, as in the AMSR-E map (Fig. 5).

It is noteworthy that the region of AMSR-E data loss near 54°S, 39°W on the west side of South Georgia Island extends more than 75 km from land because of a large iceberg that was attached to the west side of the island. A recently calved iceberg can be seen as a "protrusion" of the Antarctic ice sheet near 57°S, 47°W. The drift of both of these icebergs is clearly evident in animations of the AMSR-E data.

It is also noteworthy that the SST fronts in the clear region centered near 45°S, 60°W in the AVHRR SST gradient map are much narrower and more intense than in the AMSR-E SST gradient map. This again

front. The RTG_SST field in Fig. 6, which is based on the same in situ and AVHRR observations as the Reynolds SST field, is unexpectedly good compared with the AMSR-E. This is likely attributable to the fact that many of the meanders of the SST front in this region tend to be relatively stationary, probably due to bathymetric influence (Boebel et al. 2003).

While most of the major meanders of the SST front are evident in the RTG_SST map, its resolution limitations are readily apparent from comparisons of the RTG_SST and AMSR-E SST gradient maps in the right panels in Fig. 6. The SST gradients in the RTG_SST map are only 53% as strong as in the AMSR-E map (Fig. 5). The SST gradients in the Reynolds map are only 21% as strong.

The Brazil–Malvinas Confluence. The southwest Atlantic is a region of complex SST fronts associated

emphasizes the resolution limitation of the 56-km footprint of the AMSR-E observations.

The Gulf Stream. SST maps for the western North Atlantic are shown in Fig. 8 for 1 May 2003. The ribbon of warm water off the eastern seaboard of the United States that is evident in the AMSR-E map is the northward-flowing Florida Current, which separates from the coast near 35°N at Cape Hatteras and turns eastward to become the meandering Gulf Stream. As is typical of this region (Fig. 1), the Gulf Stream was mostly cloud covered north of about 38° in the AVHRR map. The sea surface was also obscured by clouds associated with weather systems east of Florida and in the southeast corner of the region shown in Fig. 8. The AVHRR map is thus only marginally useful during this time period.

The Reynolds SST map shows no evidence of any meanders in the Gulf Stream and provides only a blurred impression of the intense SST front associated with the Gulf Stream. The meanders are much better resolved in the RTG_SST map, but the small-scale structure is only marginally resolved throughout the region north of about 35°N. Overall, the intensities of the SST gradients are better represented in these RTG_SST and Reynolds maps of the Gulf Stream region than in the other five regions considered here but are still only 80% and 47% as strong, respectively, as in the AMSR-E map (Fig. 5).

The Kuroshio Extension. The North Pacific analogs to the Florida Current and Gulf Stream in the North Atlantic are the Kuroshio Current and its eastward extension that separates from the coast of Japan at about 35°N. SST fields for this region are shown in Fig. 9 for 10 June 2003. The AVHRR coverage during this time period was poor, but only slightly worse than average (Fig. 3). Except for rain cells near 27°N, 140°E, 24°N, 155°E, and 37°N, 178°E, the AMSR-E coverage was mostly complete during this time period.
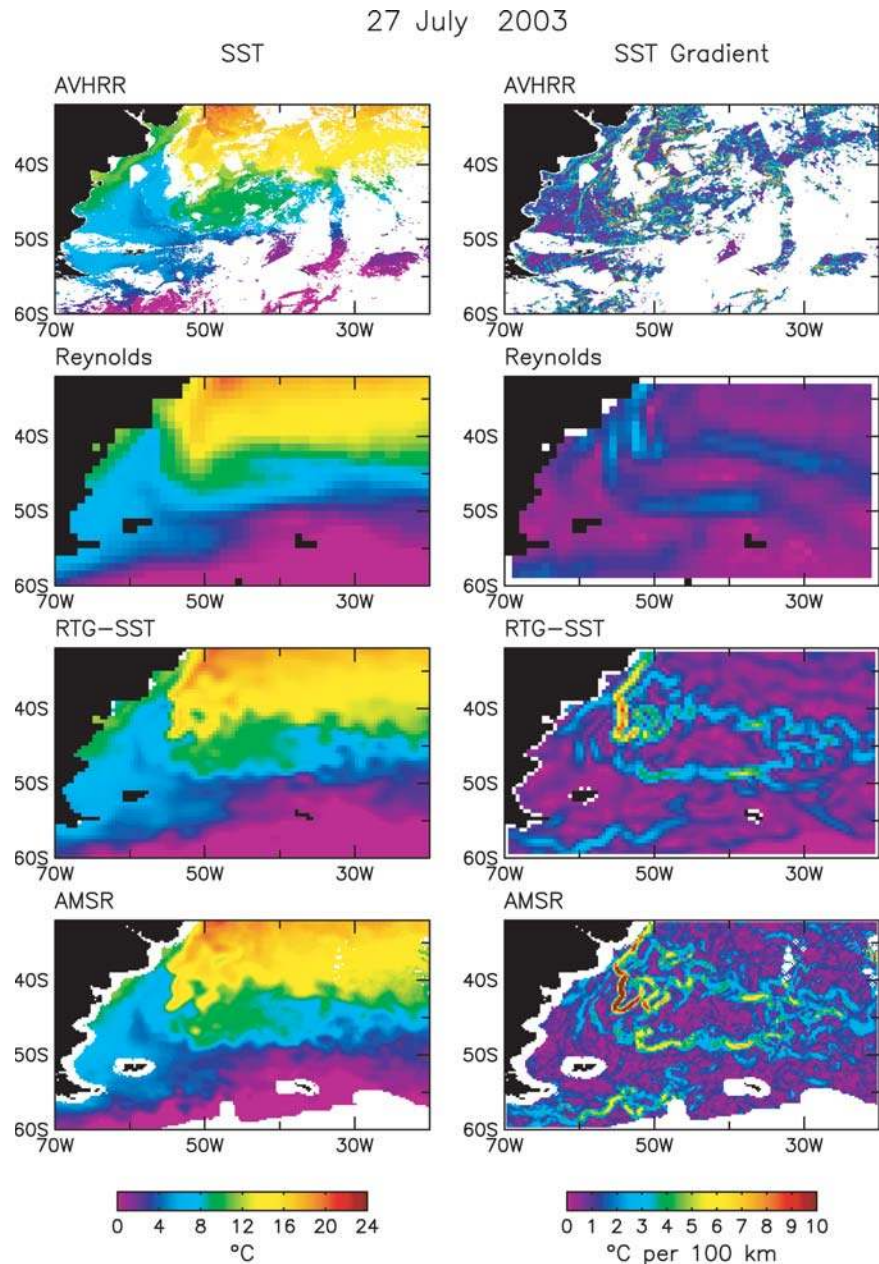

FIG. 7. Same as in Fig. 4, except for the Brazil–Malvinas Confluence region of the southwest Atlantic Ocean for the 3-day-averaging period 26–28 Jul 2003.

1 May 2003

SST — SST Gradient

AVHRR, Reynolds, RTG−SST, AMSR

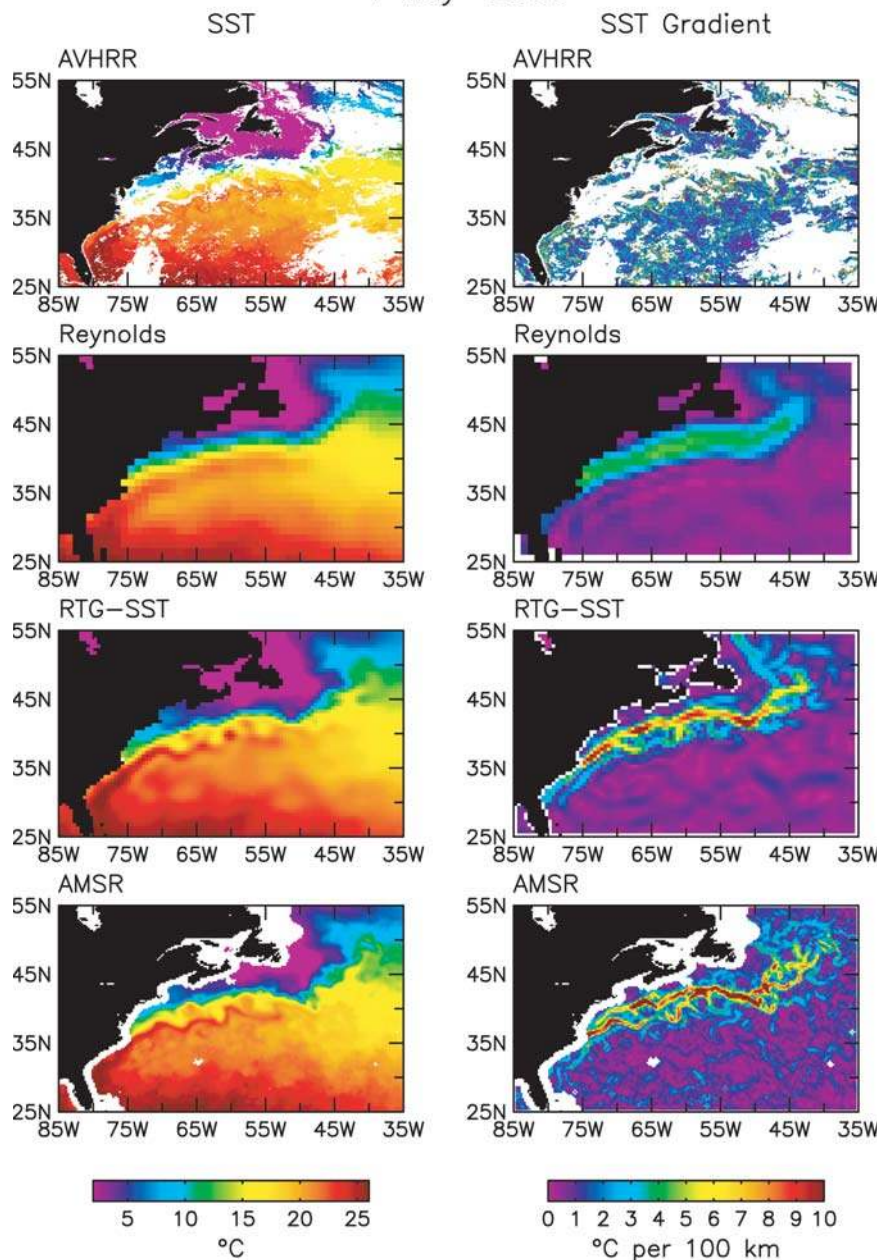°C scale: 5 10 15 20 25

°C per 100 km scale: 0 1 2 3 4 5 6 7 8 9 10

FIG. 8. Same as in Fig. 4, except for the Gulf Stream region of the western North Atlantic Ocean for the 3-day-averaging period 30 Apr–2 May 2003.

The California Current. SST maps for the California Current region of the eastern North Pacific are shown in Fig. 10 for 20 September 2002. The inadequacies of the Reynolds and RTG_SST maps are again readily apparent. Unlike the previous examples, however, serious limitations of the AMSR-E data are also evident in the California Current region. The SST fronts in this region contain numerous structures with spatial scales smaller than the 56-km footprint of the AMSR-E measurements (Strub et al. 1991). While the AMSR-E map captures the large-scale alongshore meandering of the SST front off the Oregon and California coasts, the narrow filaments of cold water that extend westward into the interior ocean and are evident in the clear regions of the AVHRR SST and SST gradient maps are poorly resolved in the AMSR-E data.

It is noteworthy that the skies were exceptionally clear during the 3-day time period considered in Fig. 10 (Fig. 3). The AVHRR coverage is highly variable in this region, depending on the extent of low-level stratus clouds that tend to form over the cold water of the California Current. Indeed, stratus clouds obscured much of the cold inshore region during the 19–21 September 2002 time period shown in Fig. 10. On the other hand, the loss of AMSR-E data near land because of contamination from the antenna sidelobes also restricts the usage of AMSR-E data to regions farther than 75 km from the coast. The use of satellite observations of SST from either IR or microwave data alone can thus be problematic for this region. The best SST fields for regions such

As in the areas considered above, the Reynolds SST map shows no evidence of the complex structures of the SST fronts east of Japan (right panels in Fig. 9). The RTG_SST map shows more of the meanders of the Kuroshio Extension but misses many of the small-scale structures of the SST fronts that are evident throughout most of the region in the AMSR-E map. The SST gradients in these RTG_SST and Reynolds maps of the Kuroshio Extension region are only 38% and 16% as strong, respectively, as in the AMSR-E map (Fig. 5).

as this are likely to be obtained from a blending of AMSR-E and AVHRR data that takes advantage of the complimentary sampling and resolution of microwave and IR measurements of SST (e.g., Guan and Kawamura 2004).

THE RESOLUTION LIMITATIONS OF REYNOLDS AND RTG_SST ANALYSES.
The improved resolution of the RTG_SST fields over the Reynolds SST fields is readily apparent from the example maps and binned scatterplots in Figs. 4–10. As summarized previously, both products are based on the same input data but differ in the details of the objective analysis procedures. The Reynolds analysis procedure apparently imposes unnecessarily heavy smoothing on the SST fields.

While they are a significant improvement over the Reynolds SST fields, the resolution of the RTG_SST fields is still coarse compared with SST fields constructed from AMSR-E data. The regions of largest resolution differences can be inferred from Fig. 11, which shows the rms differences between 3-day averages of RTG_SST and AMSR-E fields over the 12-month time period October 2002 through September 2003. In ice-free regions of the World Ocean, the largest differences, which exceed 1°C in some places, occur in regions of strong SST gradients (e.g., the Gulf Stream, the Kuroshio Extension, the eastern tropical Pacific, the Brazil–Malvinas Confluence, the ARC, and other regions of the Antarctic Circumpolar Current).

The resolution differences of the Reynolds, RTG_SST, and AMSR-E SST fields are quantified in Fig. 12, which shows the zonal wavenumber spectra of 1-month averages during the respective winter periods of 2003 for the Kuroshio Extension

region of the western North Pacific and the ARC region of the southwest Indian Ocean. The ratios of the AMSR-E to RTG_SST spectral values are about 1 down to length scales of ~400 km but increase monotonically on smaller scales (higher wavenumbers). At length scales of ~200 km, the spatial variability is less energetic in the RTG_SST fields by about a factor of 10 in the Kuroshio region and by about a factor of 100 in the ARC region. In comparison, the spatial variability is less energetic in the Reynolds SST fields by about a factor of 10 at length scales of ~400 km and by more than three orders of magnitude at length scales of ~200 km.

IMPACT OF SST SPECIFICATION ON ECMWF WIND STRESS FIELDS AT MID-LATITUDES.
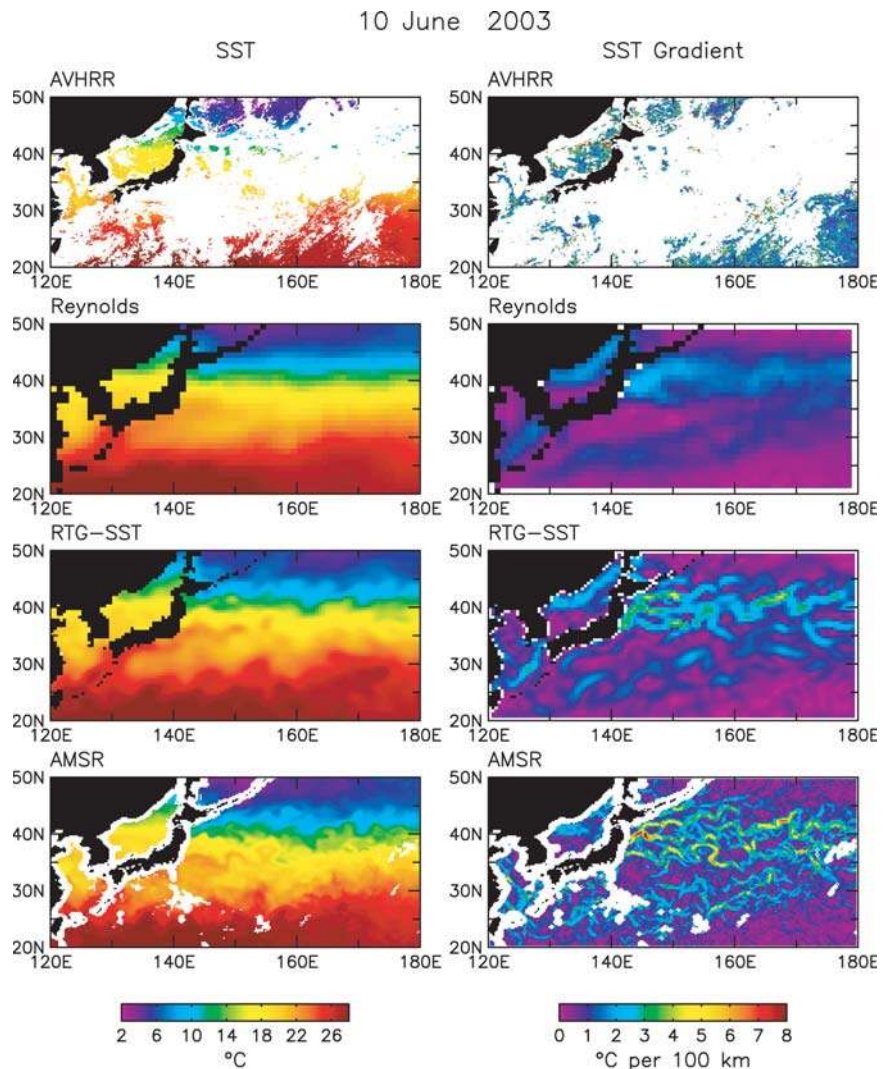The 9 May 2001 change from the Reynolds analyses to the RTG_SST analyses as

FIG. 9. Same as in Fig. 4, except for the Kuroshio Extension region of the western North Pacific Ocean for the 3-day averaging period 9–11 Jun 2003.
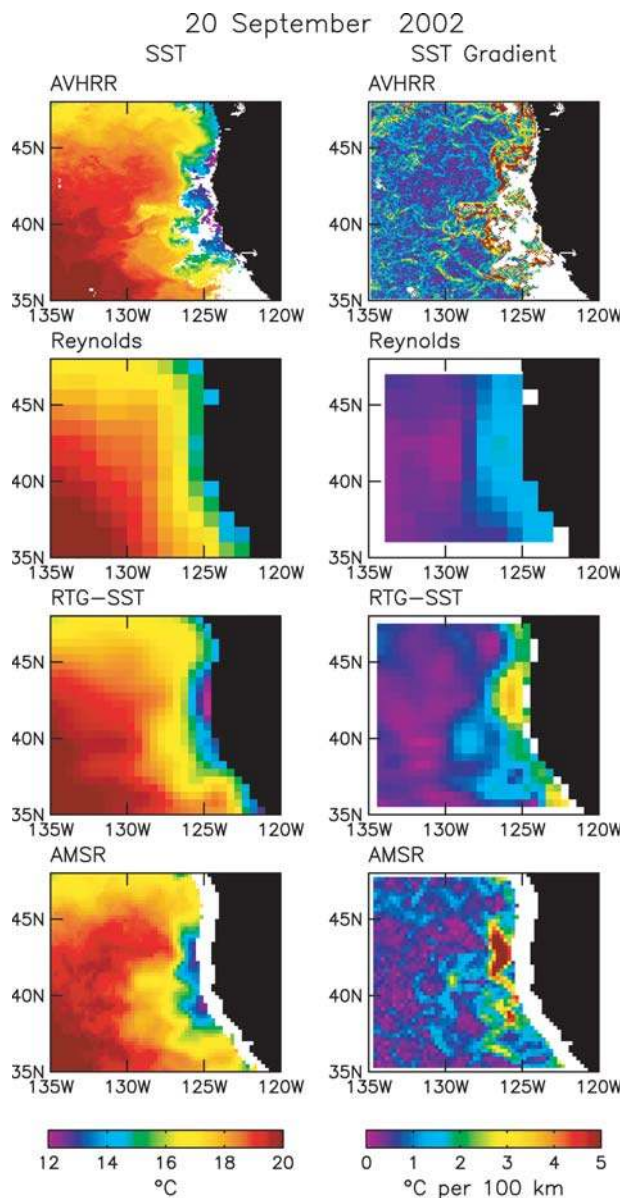
20 September 2002

FIG. 10. Same as in Fig. 4, except for the California Current region of the eastern North Pacific Ocean for the 3-day-averaging period 19–21 Sep 2002.

the ocean boundary condition in the operational ECMWF model provides an opportunity to assess the sensitivity of the model to specification of the

SST boundary condition. A recent detailed analysis of the eastern tropical Pacific region found that the wind stress fields in the ECMWF model improved dramatically after implementation of the RTG_SST boundary condition (Chelton 2005). At midlatitudes, SST effects on the surface wind field during May when the RTG_SST boundary condition was implemented are seasonally strongest in the Southern Hemisphere. The immediate impact of this change in the SST boundary condition is therefore most easily seen from analysis of the ECMWF 6-h wind stress fields[4] (more information available online at http://dss.ucar.edu/datasets/ds111.3) in the ARC region of the southwest Indian Ocean, which is the region of strongest SST influence on the surface wind field in the Southern Hemisphere midlatitude ocean (O'Neill et al. 2003).

With sufficient temporal averaging, SST effects on the wind stress field are easily distinguished from the effects of weather variability (see Fig. 8 of O'Neill et al. 2005). For present purposes, the 6-hourly ECMWF surface wind stress magnitude fields were scalar averaged over 28-day periods immediately preceding and following the week of the 9 May 2001 change of the ocean boundary condition in the ECMWF model. These 28-day periods coincide with the four 7-day-averaged Reynolds analyses before and after 9 May 2001.

The sensitivity of the ECMWF wind stress fields to specification of SST is assessed here from comparisons with the NCEP model, which continues to use the Reynolds analyses as the ocean boundary condition (B. Katz 2005, personal communication). The NCEP wind stress fields were computed from 10-m wind analyses using the wind speed–dependent drag coefficient described by Trenberth et al. (1990). The resulting wind stress magnitude fields were scalar averaged over the same two 28-day periods as the ECMWF wind stress fields. The 7-day-averaged Reynolds SST fields were averaged over both 28-day periods, and the daily averaged RTG_SST fields were averaged over the second time period.

To highlight the scales smaller than a few thousand kilometers over which SST and wind stress are highly correlated, the 28-day averaged wind stress

---

[4] The ECMWF wind stress fields analyzed here are the "accumulated stresses" over each 6-h forecast model integration period obtained from the ds111.3 data files archived at the National Center for Atmospheric Research. These forecast wind stress fields were found to be more accurate than wind stress fields computed from the 6-hourly ECMWF analyses of 10-m winds using one of the usual wind speed–dependent formulations of the drag coefficient (e.g., Trenberth et al. 1990). This is evidently due to the fact that the ECMWF 10-m wind analyses are biased low over most of the ocean by approximately 0.4 m s^{-1} relative to buoy and QuikSCAT observations (Chelton and Freilich 2005). This corresponds to an underestimate of the wind stress by 10%–20% over most of the World Ocean.

magnitude and SST fields were all spatially high-pass filtered to remove features with scales longer than 10° latitude × 30° longitude. The resulting filtered SST and wind stress magnitude fields are shown in Fig. 13. The smoothness of the Reynolds SST fields in the top two panels and the bottom panel compared with the RTG_SST field in the third panel is evident. The ECMWF and NCEP wind stress magnitude fields were very similar during the first time period. In contrast, the ECMWF wind stress magnitude field during the second time period contained much more small-scale structure than the corresponding NCEP wind stress field.
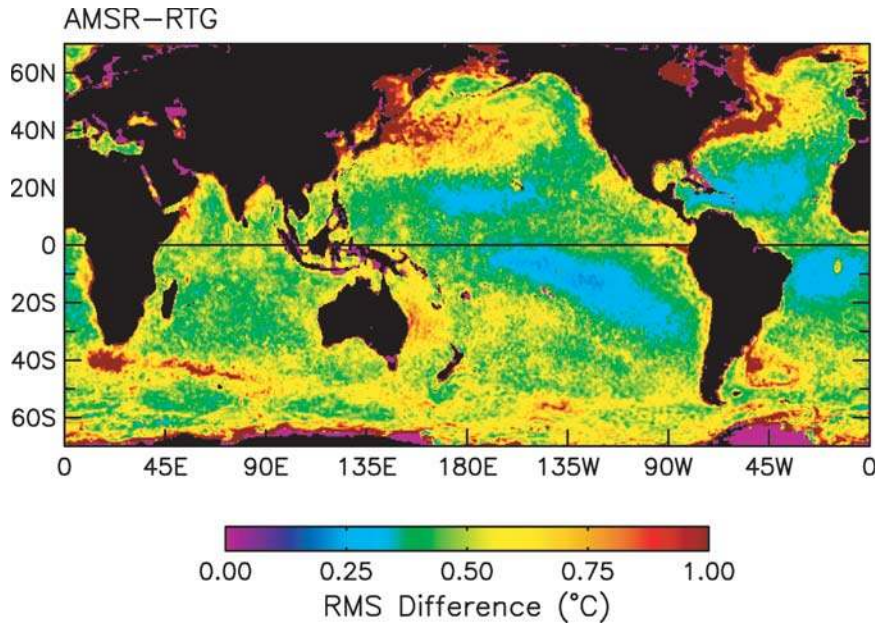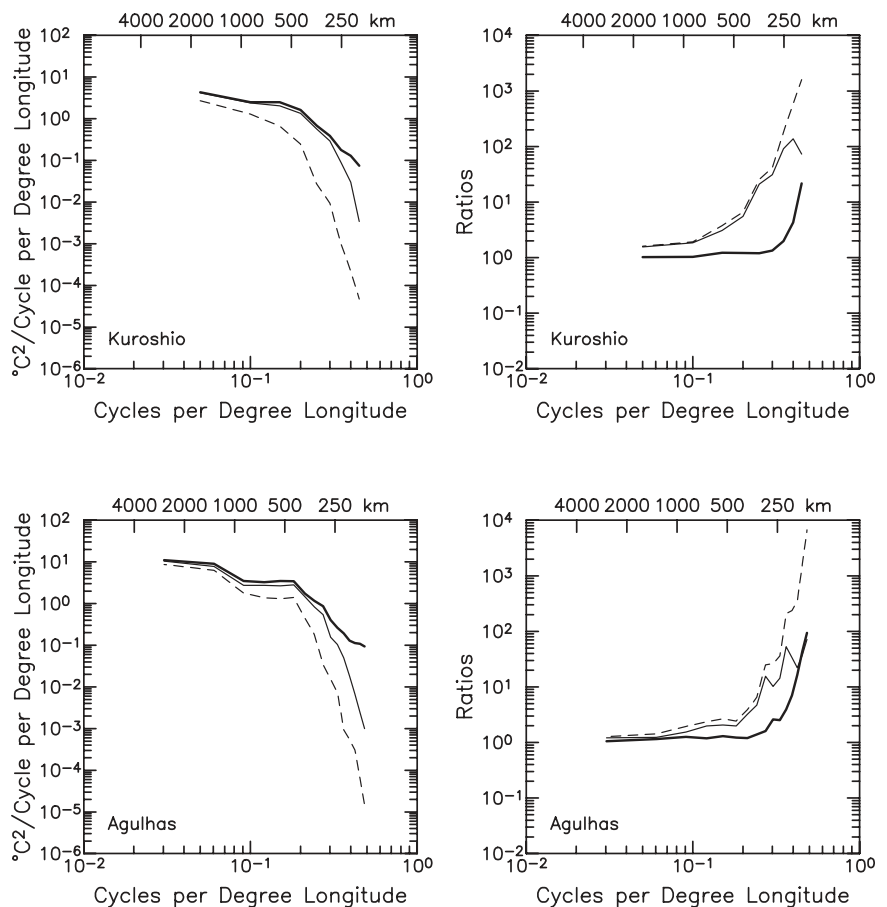

Fig. 11. Geographical distribution of the rms differences between 3-day averages of RTG_SST analyses and AMSR-E observations of SST on a 0.5° lat × 0.5° lon grid over the 12-month period Oct 2002 through Sep 2003.

Fig. 12. Zonal wavenumber power spectral density of 1-month-averaged wintertime SST fields (top) for the Kuroshio Extension region (30°–45°N, 150°–210°E) during Feb 2003 and (bottom) for the ARC region (50°–37°S, 10°–110°E) during Jul 2003. The three lines in the left panels correspond to the spectra of the AMSR-E (heavy solid lines), RTG_SST (thin solid lines), and Reynolds (dashed lines) SST fields. The three lines in the right panels correspond to the ratios of the AMSR-E to RTG_SST (heavy solid lines), RTG_SST to Reynolds (thin solid lines), and AMSR-E to Reynolds (dashed lines). The wavenumber is expressed in terms of cycles per degree of longitude on the abscissas. Corresponding selected wavelengths at the center latitude of each rectangular region are labeled along the top axes.
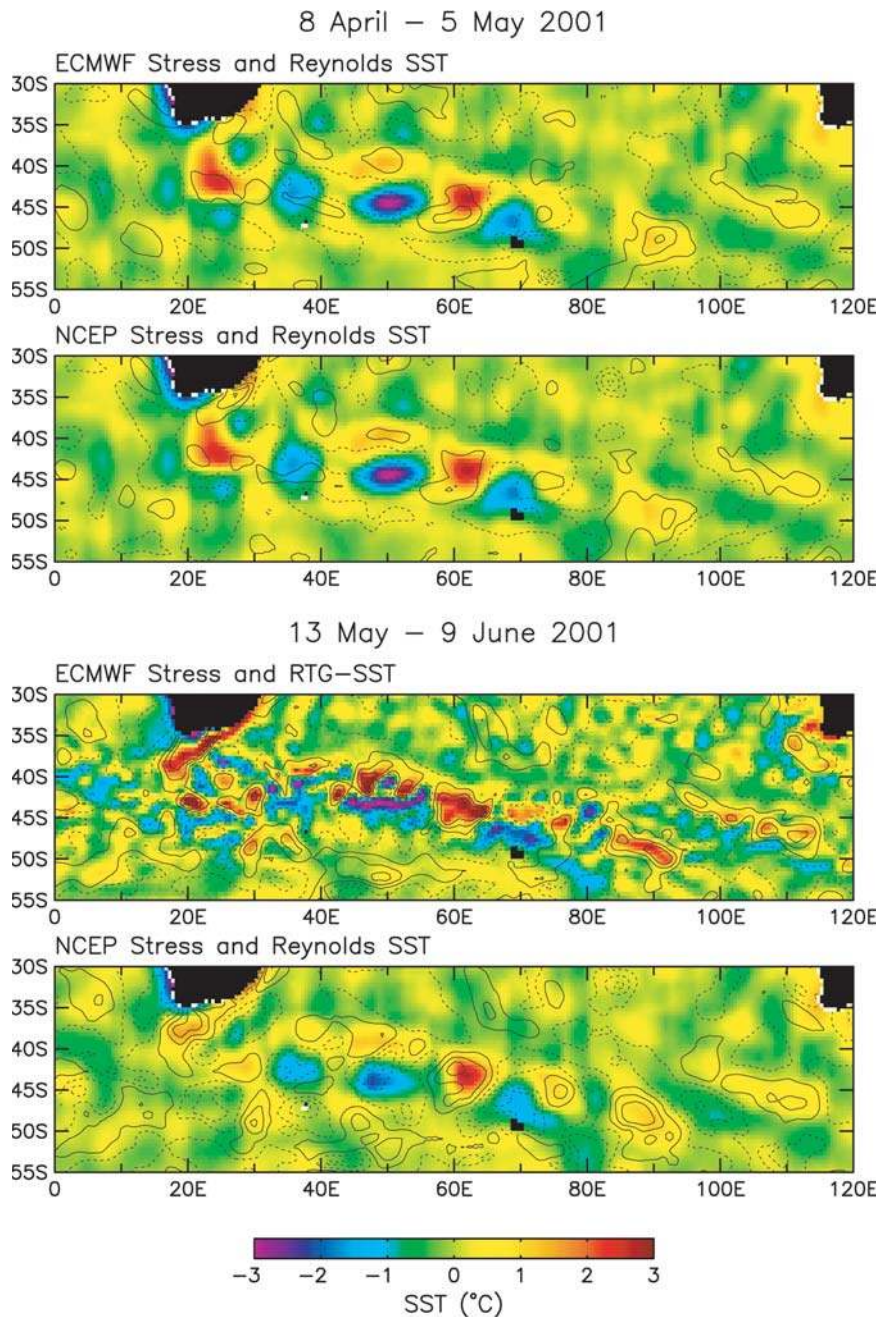
8 April — 5 May 2001

ECMWF Stress and Reynolds SST

NCEP Stress and Reynolds SST

13 May — 9 June 2001

ECMWF Stress and RTG—SST

NCEP Stress and Reynolds SST

SST (°C)

FIG. 13. Maps of spatially high-pass-filtered SST (color) and wind stress magnitude (contours, with a contour interval of 0.015 N m⁻²) in the ARC averaged over the 28-day period (top two maps) preceding and (bottom two maps) following the 9 May 2001 change of the ocean boundary condition in the ECMWF model from the Reynolds SST analyses to the RTG_SST analyses. The wind stress fields in the top and bottom maps in each pair were constructed from the ECMWF and NCEP models, respectively. The SST in each map consists of 28-day averages from the Reynolds analyses (both maps of NCEP and the top map of ECMWF) and RTG_SST analyses (the bottom map of ECMWF). The spatial high-pass filtering of these SST and wind stress magnitude fields was achieved by removing smoothed fields obtained using the multidimensional loess smoother introduced by Cleveland and Devlin (1988). The spans of the loess smoother were chosen to have half-power filter cutoffs of 10° lat × 30° lon. This is analogous to the filtering properties of 6° × 18° block averages, but the filter transfer function of the loess smoother is much better than that of block averages (see Fig. 1 of Chelton and Schlax 2003).

The remarkable fidelity with which the detailed small-scale structures in the RTG_SST field over the ARC are reproduced in the ECMWF wind stress field during the second time period is clear evidence that the improved RTG_SST boundary condition had a significant impact on the ECMWF model.

The effects of the improved SST boundary condition are quantified by the wavenumber spectra in Fig. 14. The increase in spectral energy over all wavelengths in both models from the first time period to the second time period is attributable to a general intensification of the small-scale SST structures associated with the normal seasonal increase toward the Southern Hemisphere wintertime (O'Neill et al. 2005). For the ECMWF model, the increase was a factor of 5–10 over all wavelengths smaller than 10° of longitude. In comparison, the spectral energy at these wavelengths increased by only a factor of 2–5 in the NCEP model. As the only change in the two models during this time period was the change to the RTG_SST boundary condition in the ECMWF model, the greater increase in the spectral energy at short wavelengths in the ECMWF model must be attributable to the higher resolution of the RTG_SST analyses.

The abrupt change of the ECMWF wind stress fields after the 9 May 2001 change to the RTG_SST boundary condition is also clearly apparent in the Gulf Stream region. The averages of the ECMWF and NCEP wind stress fields over the 4-week period prior to 9 May 2001 were relatively smooth, highly correlated with each other, and only moderately well correlated with the 4-week-averaged Reynolds SST field (upper two panels in Fig. 15). The 4-week-averaged NCEP wind stress field after that time is very similar in character (bottom panel in Fig. 15). In contrast, the small-scale structure in the ECMWF wind stress field increased dramatically after 9 May 2001 (third panel in Fig. 15). The small-scale features in the vicinity of the Gulf Stream are seen to be very highly correlated with small-scale features in the RTG_SST field.
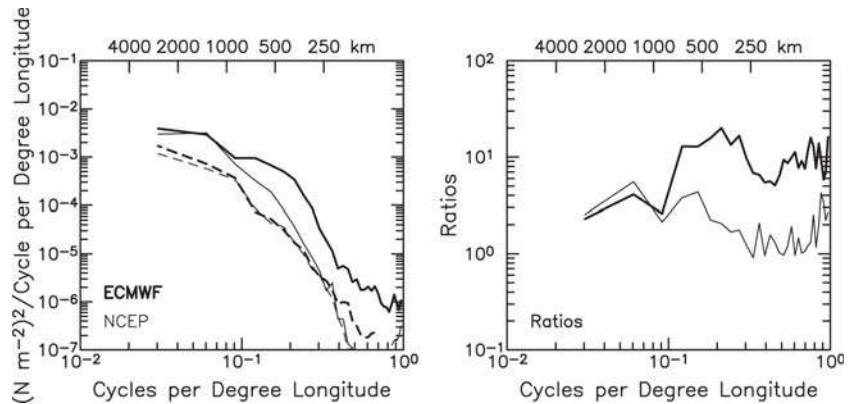

FIG. 14. Zonal wavenumber power spectral density of wind stress magnitude computed over the region 50°–37°S, 10°–110°E in the ARC from the spatially high-pass-filtered 28-day average maps shown in Fig. 13. (left) The spectra computed from the ECMWF and NCEP models (heavy and thin lines, respectively) for the 28-day-averages preceding (dashed lines) and following (solid lines) the 9 May 2001 change of the ocean boundary condition in the ECMWF model. (right) The ratios of the spectra during the second time period to the spectra during the first time period, with the heavy solid line corresponding to ECMWF and the thin solid line corresponding to NCEP. The wavenumber is expressed in terms of cycles per degree of longitude on the abscissas. Corresponding selected wavelengths at the 43.5°S center latitude of the region are labeled along the top axes.

DISCUSSION AND CONCLUSIONS. Satellite microwave measurements of SST by the TMI and AMSR-E have revealed that SST in regions of strong SST fronts associated with ocean currents exerts a strong influence on the marine atmospheric boundary layer, resulting in a remarkably high positive correlation between surface winds and SST on scales smaller than a few thousand kilometers (Xie 2004; Chelton et al. 2004). Surface winds are locally higher over warm water and lower over cool water. This coupling becomes clearly distinguishable from weather variability when the data are averaged over a few weeks or longer (O' Neill et al. 2005). Accurate knowledge of the global SST field is essential for accurate representation of this ocean–atmosphere interaction in operational NWP models, as well as in the general circulation models (GCMs) and datasets used in climate research. These applications of SST are generally based on the Reynolds SST analyses. Inadequacies of the Reynolds SST analyses have been clearly demonstrated in this paper. In most regions, SST gradients in the Reynolds SST analyses are only 15%–25% as strong as in the AMSR-E SST fields (Fig. 5).

The RTG_SST analyses that have been produced operationally by NOAA since 30 January 2001 have significantly higher resolution than the Reynolds analyses. The ECMWF operational model changed the ocean boundary condition from the Reynolds analyses to the RTG_SST analyses on 9 May 2001. Significant impacts of this change have been demonstrated from analyses of ECMWF surface wind fields in the eastern tropical Pacific (Chelton 2005), the midlatitude southwest Indian Ocean (Fig. 13), and the Gulf Stream region of the western North Atlantic (Fig. 15).

The results of this study and that of Chelton (2005) have clearly shown that the ECMWF model is sensitive to the resolution of the SST fields used as the surface boundary condition. The NCEP operational model presently continues to use the Reynolds analyses as the ocean boundary condition. Based on the analyses of the surface wind fields in the ECMWF model, it can be anticipated that the surface wind fields in the NCEP operational model would similarly change if the ocean boundary condition were changed to the RTG_SST analyses. SST specification is undoubtedly also important in the GCMs used for climate research.

The RTG_SST and Reynolds SST analyses are based on the same AVHRR and in situ observations of SST. The higher resolution of the RTG_SST fields indicates that the space–time smoothing in the Reynolds objective analysis procedure is overly con-
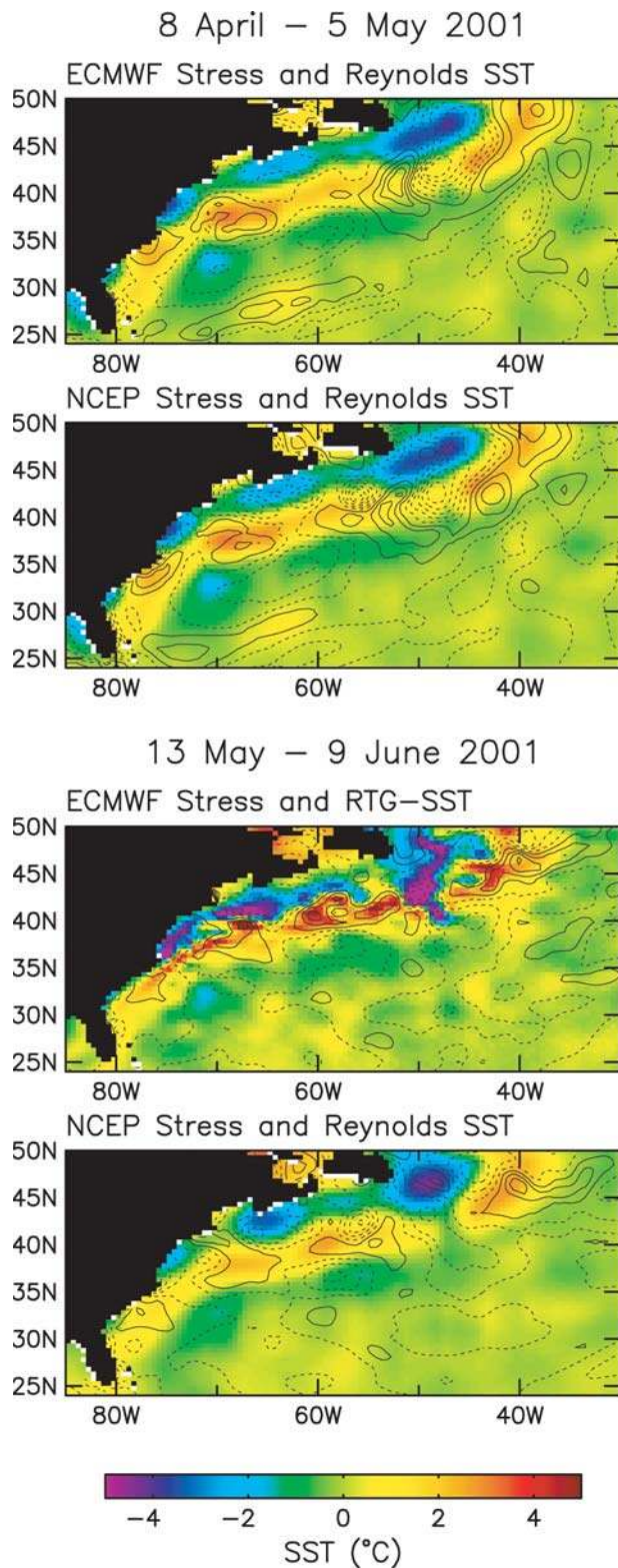
Fig. 15. Same as Fig. 13, except for the Gulf Stream region of the western North Atlantic and with a contour interval of 0.01 N m⁻² for the contours of spatially high-pass-filtered wind stress magnitude.

servative. It should be possible to perform a higher-resolution reanalysis of the historical Reynolds SST fields, which date back to November 1981, using shorter spatial correlation scales in the objective analysis scheme. Preliminary assessment of such an effort is encouraging (R. Reynolds 2005, personal communication). A 25-yr Reynolds reanalysis would be very useful for climate research.

While a significant improvement over the Reynolds analyses, the resolution of the RTG_SST analyses is inherently limited by the sparse distribution of the AVHRR and in situ data from which the SST fields are constructed. These limitations are most clearly manifest in the SST gradient fields. In most regions, SST gradients in the RTG_SST analyses are only 40%–55% as strong as in the AMSR-E SST fields (Fig. 5). Satellite microwave observations of SST by the TMI and the AMSR-E are not presently utilized in the RTG_SST analyses. Within the limitations of the ~50 km footprint of the microwave estimates of SST, and the inability to measure SST closer than about 75 km from land, the RTG_SST analyses and Reynolds reanalyses of SST could be greatly improved by inclusion of the near-all-weather and global satellite microwave observations of SST. Moreover, comparisons of contemporary TMI and AMSR-E data with AVHRR data are insightful for characterizing the errors in SST analyses for time periods before the microwave measurements of SST were available.

Looking toward the future, the AMSR-E will be succeeded by the Conical Microwave Imager/Sounder (CMIS) that is a primary sensor on the National Polar Orbiting Environmental Satellite System with a planned launch in 2009. With its full compliment of polarimetric channels, it is expected that CMIS will be able to measure SST to an accuracy at least as good as AMSR-E and with about the same footprint size and coverage.

APPENDIX: THE AMSR-E SST RETRIEVAL ALGORITHM. The sensitivity of vertically polarized brightness temperature to SST at 6.9 GHz is the basis for AMSR-E retrievals of SST. Microwave brightness temperatures also depend on the effects of wind-induced roughness on the emissivity of the

sea surface and on atmospheric temperature and moisture profiles. As the frequency and polarization dependencies on the surface roughness and the atmosphere are quite distinct from the SST dependence, the influence of these other effects can be removed based on simultaneous observations from the 10 microwave channels on the AMSR-E, corresponding to both horizontal and vertical polarization at frequencies of 6.9, 10.7, 18.7, 23.8, and 36.5 GHz.

The AMSR-E SST retrieval algorithm is a physically based two-stage regression that expresses SST in terms of the microwave brightness temperatures T_{Bi} in kelvin measured in channels i, $i=1, \ldots ,10$. Initial estimates of SST and wind speed are obtained from 21-parameter regressions,

$$p_{1j} = a_{0j} + \sum_{i=1}^{10}(a_{ij}t_i + b_{ij}t_i^2), \qquad \text{(A1)}$$

where $t_i = -\ln(290 - T_{Bi})$ for the two 23.8-GHz channels, and $t_i = T_{Bi} - 150$ for all other channels. The subscript $j = 1$ or 2 denotes SST or wind speed, respectively. The leading subscript 1 in (A1) signifies that this is the first-stage retrieval. The regression coefficients a_{ij} and b_{ij} are determined from a radiative transfer model as discussed below.

Equation (A1) provides a reasonably good initial estimate of SST and wind speed. To account for nonlinearities in the relationship between the brightness temperatures and SST and wind, a second stage to the retrieval algorithm is implemented using a large set of localized algorithms in which the retrievals are trained to perform well over a relatively narrow range of SST and wind speeds. Localized algorithms are derived for 38 SST reference values ranging from –3° to 34°C at 1°C increments and for 38 wind speed reference values ranging from 0 to 37 m s^{-1} at 1 m s^{-1} increments. All SST and wind speed combinations are considered, resulting in a two-dimensional table of 1444 localized algorithms. Each algorithm is trained to perform well over an SST range of ±1.5°C and a wind speed range of ±2 m s^{-1} centered on the reference SST and wind values.

Each localized algorithm consists of 11-parameter regressions,

$$p_{jkl} = c_{0jkl} + \sum_{i=1}^{10}c_{ijkl}t_i, \qquad \text{(A2)}$$

where the subscripts $k = -3 \ldots 34$ and $l = 0 \ldots 37$ denote the reference SST and wind speed, respectively, and the subscript $j = 1$ or 2 again denotes SST or wind speed. The second-stage retrievals p_{2j} of SST and wind speed are obtained from a bilinear interpolation of the 1444 tabulated solutions p_{jkl} obtained from (A2) for the localized algorithms that bracket the first-stage SST retrieval p_{11} and the first-stage wind speed retrieval p_{12}.

The regression coefficients c_{ijkl} in the 1444 localized algorithms were found by generating a large ensemble of simulated brightness temperatures computed from a microwave radiative transfer model (RTM) for the ocean and intervening atmosphere (Wentz and Meissner 2000) based on a set of 42,195 radiosonde soundings launched from weather ships and small islands around the global ocean (Wentz 1997). The radiosondes were used to specify the atmospheric part of the RTM. For each radiosonde, the sea surface wind speed was varied from 0 to 40 m s^{-1}, wind direction was varied over the full 360° range, and sea surface temperature was varied ±5.5°C about the climatological average Reynolds SST for the location of the radiosonde. For each of these simulated Earth scenes, the set of 10 AMSR-E brightness temperatures was computed by the RTM, and noise was added to simulate sensor noise. The simulated brightness temperatures were substituted into (A1), and the regression coefficients a_{ij} and b_{ij} in the first-stage algorithms were determined by least-squares minimization.

The regression coefficients c_{ijkl} for the 1444 localized algorithms given by (A2) were determined similarly by least-squares minimization. Each localized algorithm was trained using only the small subset of the simulated Earth scenes with SST and wind speed values that fell within the ±1.5°C and ±2 m s^{-1} window centered on the algorithm's reference SST and wind speed.

For the present study, only the AMSR-E retrievals of SST are considered. The accuracy was assessed from comparisons with TMI estimates of SST. A more complete analysis of the AMSR-E measurement accuracy based on direct comparisons with buoys is underway. The differences between TMI and the Tropical Atmosphere–Ocean (TAO) buoy measurements of SST have previously been shown to have a mean of –0.08°C and a standard deviation of 0.57°C (Gentemann et al. 2004). The corresponding rms difference of 0.58°C is an upper bound on the errors of the TMI measurements of SST. Taking into account the differences owing to the fact that TMI measurements consist of the average temperatures in the upper millimeter over a 46-km footprint and the TAO measurements consist of temperatures at 1-m depth at a point location, the TMI measurement accuracy is estimated to be about 0.5°C.

The differences between collocated (within 25 km and 3 h) TMI and AMSR-E measurements of SST computed from the first year of the AMSR-E dataset have a mean of 0.06°C and a standard deviation of 0.56°C. The rms difference is therefore 0.57°C. For SST ranging from 11° to 28°C, over which 83% of the collocations occurred, there is negligible SST dependence of the differences between AMSR-E and TMI estimates of SST. There were very few collocations in SST cooler than 11°C because of the limited latitudinal range sampled by TMI. At temperatures higher than 28°C, the TMI estimates become biased high relative to AMSR-E by as much as 0.55°C. We believe this bias is attributable to small systematic errors in TMI estimates of these high SSTs.

With a TMI measurement accuracy of 0.5°C, and assuming that the TMI and AMSR-E measurement errors are independent, the rms difference of 0.57°C corresponds to an AMSR-E measurement error of about 0.3°C. This is probably an underestimate since the errors in collocated measurements by TMI and AMSR-E may be somewhat correlated because errors in the environmental correction that are responsible for the SST estimation errors are similar for both instruments. We therefore suggest that the AMSR-E measurement error for a single observation is about 0.4°C. When averaged over time, as in the examples in the figures in this paper, these errors are reduced.

REFERENCES

Boebel, O., T. Rossby, J. Lutjeharms, W. Zenk, and C. Barron, 2003: Path and variability of the Agulhas Return Current. *Deep-Sea Res.,* **50B,** 35–56.

Cayula, J.-F., and P. Cornillon, 1996: Cloud detection from a sequence of SST images. *Remote Sens. Environ.,* **55,** 80–88.

Chelton, D. B., 2005: The impact of SST specification on ECMWF surface wind stress fields in the eastern tropical Pacific. *J. Climate,* **18,** 530–550.

——, and M. G. Schlax, 2003: The accuracies of smoothed sea surface height fields constructed from tandem altimeter datasets. *J. Atmos. Oceanic Technol.,* **20,** 1276–1302.

——, and M. H. Freilich, 2005: Scatterometer-based assessment of 10-m wind analyses from the ECMWF and NCEP numerical weather prediction models. *Mon. Wea. Rev.,* **133,** 409–429.

——, F. J. Wentz, C. L. Gentemann, R. A. de Szoeke, and M. G. Schlax, 2000: Microwave SST observations of transequatorial tropical instability waves. *Geophys. Res. Lett.,* **27,** 1239–1242.

——, and Coauthors, 2001: Observations of coupling between surface wind stress and sea surface temperature in the eastern tropical Pacific. *J. Climate,* **14,** 17 877–17 904.

——, M. G. Schlax, M. H. Freilich, and R. F. Milliff, 2004: Satellite measurements reveal persistent small-scale features in ocean winds. *Science,* **303,** 978–983.

Cleveland, W. S., and S. J. Devlin, 1988: Locally weighted regression: An approach to regression analysis by local fitting. *J. Amer. Stat. Assoc.,* **83,** 596–610.

Diaz, J. P., M. Arbelo, F. J. Expósito, G. Podestá, J. M. Prosperio, and R. Evans, 2001: Relationship between errors in AVHRR-derived sea surface temperature and the TOMS aerosol index. *Geophys. Res. Lett.,* **28,** 1989–1992.

Di Vittorio, A. V., and W. J. Emery, 2002: An automated dynamic threshold cloud-masking algorithm for daytime AVHRR images over land. *Trans. Geosci. Remote Sens.,* **40,** 1682–1694.

Gentemann, C. L., F. J. Wentz, C. A. Mears, and D. K. Smith, 2004: In situ validation of Tropical Rainfall Measuring Mission microwave sea surface temperatures. *J. Geophys. Res.,* **109,** C04021, doi:10.1029/2003JC002092.

Guan, L., and H. Kawamura, 2004: Merging satellite infrared and microwave SSTs: Methodology and evaluation of the new SST. *J. Oceanogr.,* **60,** 905–912.

Hashizume, H., S.-P. Xie, W. T. Liu, and K. Takeuchi, 2001: Local and remote atmospheric response to tropical instability waves: A global view from space. *J. Geophys. Res.,* **106,** 10 173–10 185.

Legeckis, R., 1977: Long waves in the eastern equatorial Pacific Ocean: A view from a geostationary satellite. *Science,* **197,** 1179–1181.

Mantua, N. J., S. R. Hare, Y. Zhang, J. M. Wallace, and R. C. Francis, 1997: A Pacific interdecadal climate oscillation with impacts on salmon production. *Bull. Amer. Meteor. Soc.,* **78,** 1069–1079.

Okumura, Y., S.-P. Xie, A. Numaguti, and Y. Tanimoto, 2001: Tropical Atlantic air–sea interaction and its influence on the NAO. *Geophys. Res. Lett.,* **28,** 1507–1510.

O'Neill, L. W., D. B. Chelton, and S. K. Esbensen, 2003: Observations of SST-induced perturbations of the wind stress field over the Southern Ocean on seasonal time scales. *J. Climate,* **16,** 2340–2354.

——, ——, ——, and F. J. Wentz, 2005: High-resolution satellite measurements of the atmospheric boundary layer response to SST variations along the Agulhas Return Current. *J. Climate,* in press.

Qiao, L., and R. H. Weisberg, 1995: Tropical instability wave kinematics: Observations from the Tropical Instability Wave Experiment. *J. Geophys. Res.,* **100,** 8677–8693.

Reynolds, R. W., and T. M. Smith, 1994: Improved global sea surface temperature analyses using optimum interpolation. *J. Climate,* **7,** 929–948.

——, N. A. Rayner, T. M. Smith, D. C. Stokes, and W. Wang, 2002: An improved in situ and satellite SST analysis for climate. *J. Climate,* **15,** 1609–1625.

Saraceno, M., C. Provost, A. R. Piola, J. Bava, and A. Gagliardini, 2004: Brazil Malvinas Frontal System as seen from 9 years of advanced very high resolution radiometer data. *J. Geophys. Res.,* **109,** C05027, doi:10.1029/2003JC002127.

Stowe, L. L., P. A. Davis, and E. Paul McClain, 1999: Scientific basis and initial evaluation of the CLAVR-1 global clear/cloud classification algorithm for the Advanced Very High Resolution Radiometer. *J. Atmos. Oceanic Technol.,* **16,** 656–681.

Strub, P. T., P. M. Kosro, and A. Huyer, 1991: The nature of the cold filaments in the California Current System. *J. Geophys. Res.,* **96,** 14 743–14 768.

Thiébaux, J., E. Rogers, W. Wang, and B. Katz, 2003: A new high-resolution blended real-time global sea surface temperature analysis. *Bull. Amer. Meteor. Soc.,* **84,** 645–656.

Tomita, T., S.-P. Xie, and M. Nonaka, 2002: Estimates of surface and subsurface forcing for decadal sea surface temperature variability in the midlatitude North Pacific. *J. Meteor. Soc. Japan,* **80,** 1289–1300.

Trenberth, K. E., W. G. Large, and J. G. Olson, 1990: The mean annual cycle in global ocean wind stress. *J. Phys. Oceanogr.,* **20,** 1742–1760.

Visbeck, M., P. Chassignet, R. G. Curry, T. L. Delworth, R. R. Dickson, and G. Krahmann, 2003: The ocean's response to North Atlantic Oscillation variability. *North Atlantic Oscillation: Climatic Significance and Environmental Impact, Geophys. Monogr.,* No. 134, Amer. Geophys. Union, 113–145.

Wentz, F. J., 1997: A well-calibrated ocean algorithm for SSM/I. *J. Geophys. Res.,* **102,** 8703–8718.

——, and. T. Meissner, 2000: Algorithm Theoretical Basis Document (ATBD), version 2. AMSR-E Ocean Algorithm, Remote Sensing Systems Tech. Rep. RSS 121599A-1, 55 pp. [Available online at www.remss.com/papers/AMSR-E_Ocean_Algorithm_Version_2.doc).

——, C. Gentemann, D. Smith, and D. Chelton, 2000: Satellite measurements of sea surface temperature through clouds. *Science,* **288,** 847–850.

Xie, S.-P., 2004: Satellite observations of cool ocean–atmosphere interaction. *Bull. Amer. Meteor. Soc.,* **85,** 195–208.